Journal of Basic Physical Research ISSN: 2141-8403 Prints, 2141-8411 Online
Vol.15, Issue 1, March, 2026, pp. 14– 34, Available online at https://journals.unizik.edu.ng/jbpr/

MAPPING MINERALIZED POTENTIAL AREAS USING INTEGRATED GEOPHYSICAL AND GEOCHEMICAL TECHNIQUES IN PART OF ILORIN SHEET 223, SOUTHWESTERN NIGERIA

Olaiya Moshood Lekan[1], Jimoh Ajadi[1] and Gabriel Efomeh Omolaiye[1],
[1]*Department of Geology and Mineral Science, Kwara State University, Malete, Kwara State, Nigeria*
Olaiya Moshood Lekan: olaiyamoshoodlekan@gmail.com
Jimoh Ajadi: jimoh.ajadi@kwasu.edu.ng
Gabriel Efomeh Omolaiye: gabriel.omolaiye@kwasu.edu.ng

Abstract
This study employs an integrated geophysical and geochemical approach to delineate mineralized zones in part of Ilorin Sheet 223, southwestern Nigeria. Advanced filtering and transformation techniques were applied to the high-resolution aeromagnetic data, this includes reduction to the equator (RTE), analytic signal amplitude (AS), tilt derivative (TDR), total horizontal derivative (THDR), first vertical derivative (FVD), source parameter imaging (SPI), and Euler deconvolution techniques, revealing a structurally complex terrain dominated by NE-SW and NW-SE lineaments, shallow magnetic sources (60–350 m depth). Aeroradiometric analysis, which consist of ternary maps and K/Th and K/U ratios, highlighted potassic alteration and radioelement enrichments associated with felsic granites and pegmatites. Soil geochemical analysis of 49 samples for 13 trace elements (Li, Rb, Cs, Nb, Ta, Sn, Cu, U, Th, Pb, Zn, Fe, La) using XRF, analyzed with statistical analysis including univariate and multivariate statistics, identified log-normal distributions, element correlation that reveal strong element associations, and three principal factors were observed: (1) Fe-Cu-Zn-U (hydrothermal/supergene), (2) Li-Cs-Nb-Ta-Sn-Rb (LCT pegmatite-related), and (3) Th-La-Pb-U (REE-radiogenic). Integration of these datasets delineates high-priority polymetallic targets in the northeastern (Elesin-Funfun/Alayin), western (Oniguguru/Oniyere/Ahogbada), and southeastern (Erin-Ile) sectors, controlled by structural intersections and hydrothermal alteration. The results provide a robust, multi-parameter exploration model that reduces target ambiguity and highlights the prospectivity for polymetallic mineralization, supporting sustainable resource development in the study area.
Keywords*: Mineralization Potential Mapping; Aeromagnetic Interpretation; Aero-radiometric Analysis; Geochemical Soil Anomalies.*

Introduction

The increasing importance of mineral resources in industrial development, technological innovation, and energy transition has intensified the need for efficient and sustainable exploration strategies. Mineral commodities such as lead, zinc, iron, and gold play a vital role in supporting modern infrastructure and manufacturing sectors, making their accurate discovery and evaluation essential (El-Omairi *et al*., 2025; Shereif *et al*., 2025). However, conventional exploration approaches that rely heavily on surface geological mapping are often insufficient to detect concealed mineral deposits, especially in structurally complex or poorly accessible terrain (Upadhyay, 2025). This limitation has driven the adoption of integrated exploration techniques that provide reliable subsurface information and improve targeting accuracy (Ebele *et al*., 2025).

Among these techniques, aeromagnetic and aeroradiometric surveys have become essential tools in regional mineral exploration due to their ability to rapidly characterize subsurface conditions over large areas. Aeromagnetic data are highly effective for mapping lithological variations and structural trends such as faults, fractures, and shear zones. These structures frequently serve as conduits for mineralizing fluids and play a major role in controlling the emplacement of ore deposits. (Abdelrady et al., 2023; Shereif et al., 2025). In addition, aeroradiometric data provide information on the spatial distribution of naturally occurring radioactive elements, including potassium (K), uranium (U), and thorium (Th), which are

widely used as indicators of lithological differences and hydrothermal alteration related to mineralization processes (Ebele et al., 2025; Jahantigh et al., 2025).

Despite their effectiveness in delineating subsurface features, geophysical datasets alone may not serve as a stand-alone tool in detecting anomalies directly related to economic mineralization. Geochemical methods, particularly soil geochemistry, provide essential validation by detecting elemental anomalies and surface dispersion patterns associated with subsurface mineral deposits. Analysis of major and trace elements enables differentiation between background concentrations and geochemically anomalous zones associated with ore-forming processes, thereby improving exploration reliability (El-Raouf et al., 2023; Xie et al., 2023). The integration of geochemical data with aeromagnetic and aeroradiometric interpretations, therefore, enhances confidence in mineral potential assessments and reduces the risk of false exploration targets.

There is a record of previous studies on Ilorin Sheet 223, in which researchers have utilised geophysical methods to map basement structures and geochemical surveys to identify trace-element anomalies, each independently. There remains a knowledge gap in the integration of these datasets for targeted mineralisation mapping in unexplored areas, such as the selected area in Ilorin Sheet 223. This gap limits the precision of exploration in Precambrian terrains, where structural controls and hydrothermal alterations are key to ore deposition and are obscured by weathering and vegetation. The present study bridges this knowledge gap by combining high-resolution aeromagnetic, aeroradiometric, and soil geochemical analyses to create a multi-layered model that correlates subsurface structures with surface anomalies, thereby advancing sustainable exploration practices in the Nigerian Basement Complex.

The primary aim of this research is to delineate potential mineralized zones in selected parts of Ilorin Sheet 223, southwestern Nigeria, through the integrated analysis of aeromagnetic, aeroradiometric, and geochemical datasets. This aim shall be achieved through; processing and interpretation of aeromagnetic data for identifying subsurface structural trends, that may control mineralization, analyze aeroradiometric data for mapping radioelement distributions and hydrothermal alteration zones indicative of mineralization, conduct soil geochemical sampling and statistical analysis to detect elemental anomalies and associations linked to mineralization, and integrate geophysical and geochemical findings to correlate structural features with geochemical signatures, thereby prioritizing high-potential zones.

Geology and accessibility of the Area

The study area, located in part of Ilorin Sheet 223 and bounded by latitudes 8°6′N to 8°9.6′N and longitudes 4°31.2′E to 4°43.2′E (covering approximately 146.4 km² in Kwara State, southwestern Nigeria), encompasses towns such as Offa, Erin-Ile, Ilemona, Alayin, Oniuguru, Oniyere, Elesin-Funfun, Aho Igbada, Alata, and Ira, with good accessibility via road networks.

Geologically, the investigated region is situated within the Nigerian Basement Complex, representing a reactivated portion of the Precambrian Pan-African Mobile Belt. The study area consists of intensely deformed migmatites, gneisses (encompassing banded and augen types), schists, quartzites, pegmatites, and granitic bodies ranging from porphyritic to fine-grained textures, all influenced by repeated orogenic episodes, formed from the Pan-African orogeny (Rahaman, 1988; Dada, 1998; Okunlola et al., 2022; Adebayo et al., 2023; Kanmi et al., 2024). The study area (Figure 1) is primarily characterized by migmatites and gneisses, which display paleosomes, neosomes, both ductile and brittle deformations, layered felsic-mafic sequences, and augen structures involving quartz and feldspar. Less prominent rock units consist of quartz-schists, marble, and sporadic diorite deposits. Key structural elements, such as faults,

shear zones, folds, foliations, and lineaments oriented mainly NE–SW and NW–SE, exert significant influence over mineral deposition, river systems, and subsurface water movement. Surface-exposed pegmatite veins are notable in the vicinity of Alayin, Ahogbada, and Aboto-Afa, near Elesin Funfun. Generally, Ilorin sheet 223 has been recognized to possess a vast rare-metal pegmatite, forming part of the larger Pan-African belts that contain Lithium-Cesium-Tantalum (LCT)-type pegmatites abundant in strategic minerals like lithium (in forms such as spodumene and lepidolite), tantalite-columbite, cassiterite, tin, rare-earth elements, beryl, and various gemstones (Garba, 2003; Okunlola, 2005; Okunlola and Somorin, 2006). In addition, records indicate the presence of iron ore, tourmaline, mica, kaolin, quartz, marble, and feldspar, highlighting the area's diverse metallic resources (Adubifa, 2019; Tanko et al., 2024).

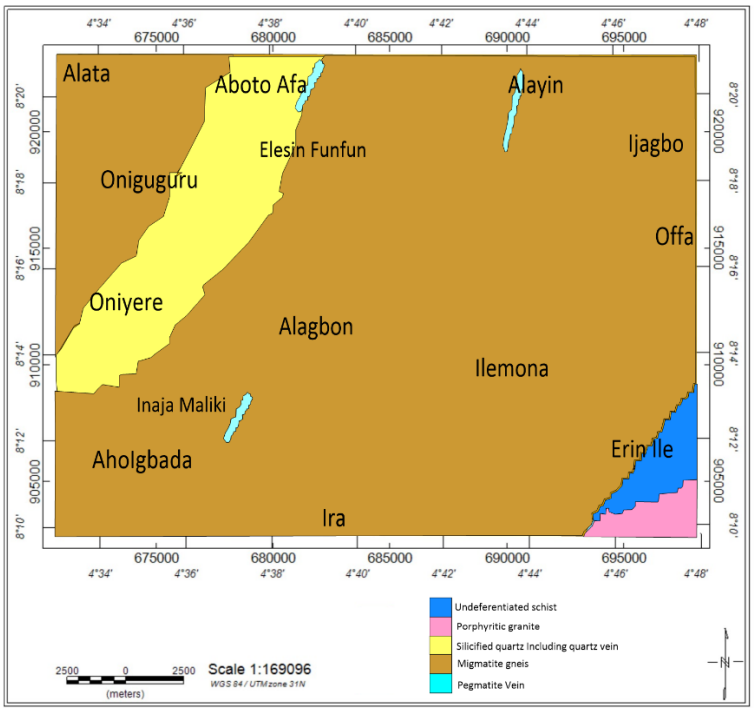

Figure 1: Location and Geologic map of the Study Area

Materials and Methods

The materials used in this research consist of airborne geophysical datasets and soil geochemical samples. Aeromagnetic and aeroradiometric datasets were obtained from the Nigerian Geological Survey Agency. The datasets were acquired during regional airborne geophysical surveys and provided high-resolution information on subsurface magnetic and radiometric characteristics.

Aeromagnetic data processing was carried out using Oasis Montaj software. The total magnetic intensity data were corrected for the International Geomagnetic Reference Field to obtain residual magnetic intensity data. Several enhancement filters were applied including reduction to the equator, total horizontal derivative, first vertical derivative, analytic signal, tilt derivative, source parameter imaging, and Euler deconvolution. These filters help highlight structural features and estimate depths to magnetic sources. Radiometric data processing involved the analysis of potassium, uranium, and thorium channels. Ternary maps were produced to visualize the combined distribution of the three radioelements. Elemental ratio maps such as K/Th and K/U were also generated to identify zones of hydrothermal alteration. Soil geochemical sampling was carried out across the study area with emphasis on the B-horizon of the soil profile. A total of 49 soil samples were collected and analyzed using X-ray fluorescence techniques. The elements analyzed include

Li, Fe, Rb, Cs, Nb, Ta, Sn, Cu, U, Th, Pb, Zn, and La. Statistical analyses such as descriptive statistics, correlation analysis, and factor analysis were applied to interpret the geochemical data.

.

Results and Discussion

Aeromagnetic Data

Total Magnetic Intensity

The Total Magnetic Intensity map (Figure 2) shows a highly heterogeneous magnetic basement, with values ranging from −155 to 80 nT. Prominent, elongated high-amplitude anomalies concentrated in the central and eastern sectors are attributed to shallow, strongly magnetized mafic–ultramafic intrusions or magnetite-rich basement rocks, emplaced or reactivated along NE–SW and NW–SE shear zones that may localize hydrothermal alteration and mineralization. In contrast, broad low-amplitude anomalies, mainly in the north and locally in the south, are linked to weakly magnetized felsic plutons, thick weathered regolith or sedimentary cover occupying structural depressions between more magnetic belts. The variation belts of highs and lows delineate major structural framework of the area and characterizing its basement systems.

The Residual Magnetic Map

The residual magnetic intensity map (Figure 3), derived from regional-residual separation of aeromagnetic data, isolates short-wavelength anomalies ranging from −88.34 to +94.17 nT. These anomalies reveal a highly heterogeneous magnetic basement characterized by alternating positive and negative domains. Dominant elongated positive anomalies, concentrated in the central-northern sectors, form curvilinear to lobate shapes are attributed to shallow, strongly magnetized mafic-ultramafic intrusions. Sharp bipolar patterns indicate near-vertical lithological contacts or dykes (Grant, 1985; Reeves, 2005). In contrast, broad negative anomalies in the western and southern parts correspond to weakly magnetized migmatite-gneiss complexes, felsic granitic plutons, or hydrothermally demagnetized zones (Airo, 2015).

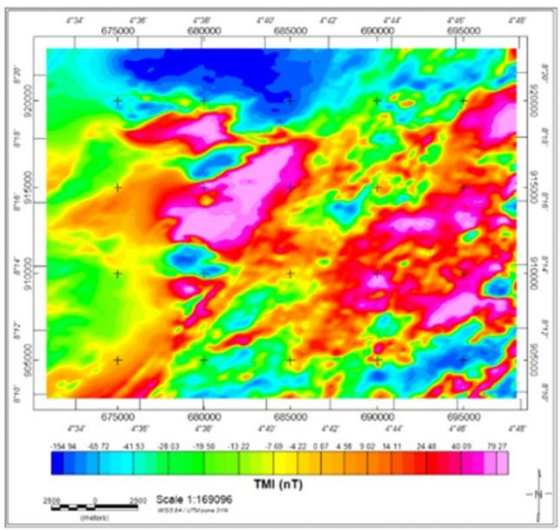

Figure 2: Total Magnetic Intensity (TMI) map of the Study Area

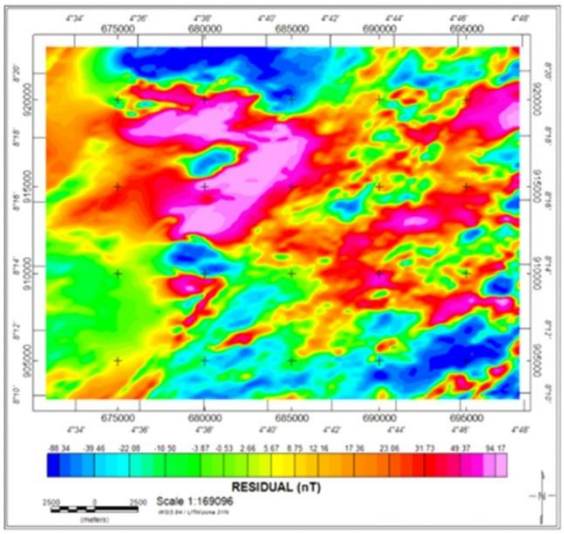

Figure 3: Residual Magnetic Intensity (RMI) map of the Study Area

Reduction to Equator Map

The reduction to the equator (RTE) map (Figure 4) corrects for low magnetic latitude effects yielding symmetric anomalies centered over magnetic sources with values ranging from −123 to +46 nT. Positive anomalies dominate central-eastern sectors, with NE-SW trending features attributed to ultramafic rocks consisting of Iron rich and other metallic mineral deposit (Ekwume *et al.,* 1995, Okunlola. 2008). Negative anomalies in western/southern areas

correspond to migmatite-gneiss complexes, felsic granites, or demagnetized zones. Sharp gradients delineate shear zones, faults, and lithological contacts.

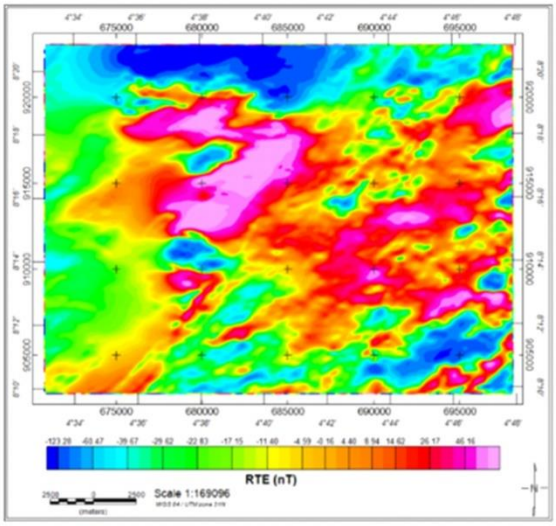

Figure 4: Reduction to Equator (RTE) map of the Study Area

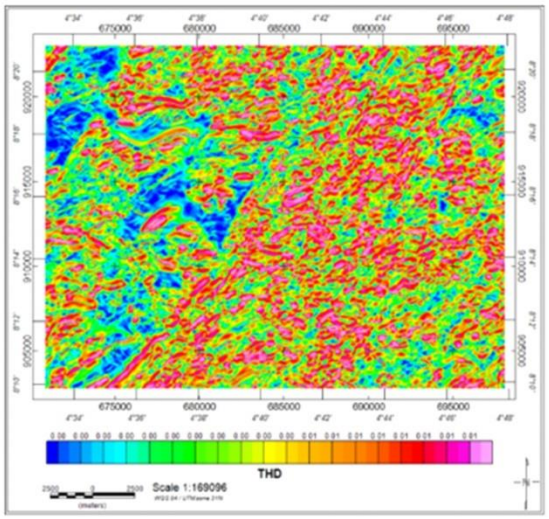

Figure 5: Total Horizontal Derivative (THD) map of the Study

Total Horizontal Derivative (THD) Map

Figure 5 shows the THD map with values ranges between 0.00 to 0.01 nT. This enhances horizontal magnetic gradients to identify subsurface edges. High THD values form dense, curvilinear ridges, marking sharp lithological contacts, and discontinuities. Low values indicate homogeneous domains within broader units. High-gradient ridges suggest potential structural controls on mineralization, including magnetite-rich zones (iron), ultramafic-hosted chromite/nickel-PGE, and shear-zone traps for hydrothermal deposits (Holden *et al*., 2008; Airo, 2015). Contacts between high- and low-gradient domains are prospective for pegmatite-related associated rare metals as these bodies often intrude along lithological or structural boundaries (Partington & Williams, 2000).

First Vertical Derivative (FVD)

The First Vertical Derivative (FVD) map (Figure 6) derived from residual magnetic intensity. The FVD values range from -0.18 nT (blue/cyan) to +0.12 nT (pink/red/magenta), with positive values highlighting high magnetic intensity especially in the southeast, central, extreme northwest, and northeast portions, indicating zones of high magnetic susceptibility interpreted as mineralized fractures, faults, and dykes potentially enriched with iron ore and other metallic minerals (Okunlola., 2008). These zones exhibit high structural density in the NW, NE, and SE sectors, with prominent linear features trending NE–SW (dominant), N–S, E–W, and NW–SE. The overall chaotic, high-frequency pattern reflects a structurally complex basement terrain with numerous shallow magnetic sources, suggesting favorable prospects for metallic (Airo, 2015; Reeves, 2005).

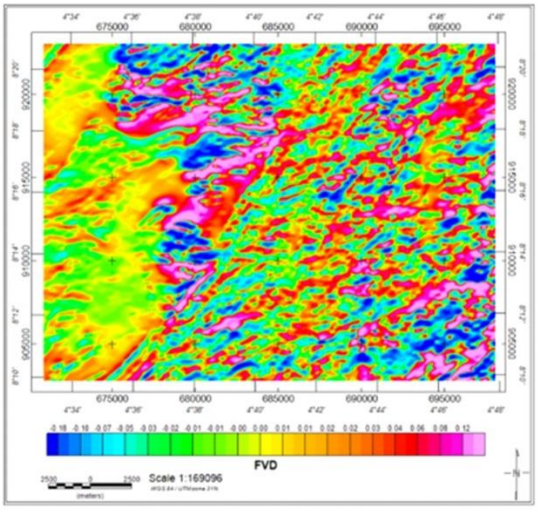

Figure 6: First Vertical Derivative (FVD) map of the Study Area

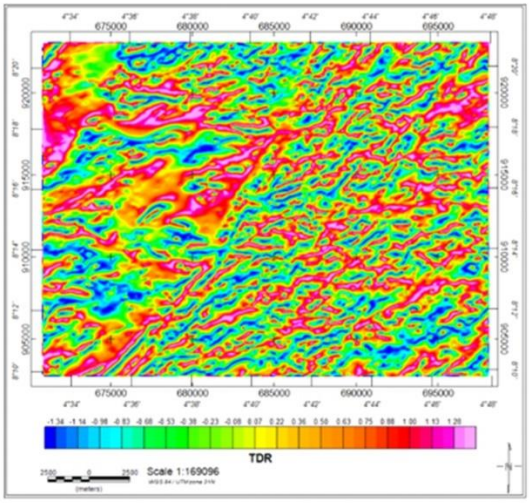

Figure 7: Tilt Derivative (TDR) map of the Study Area

Tilt Derivative (TDR) Map

The tilt derivative (TDR) map (Figure 7) with values ranging between −1.34 to +1.28 radians. This normalizes the vertical derivative by the total horizontal gradient, enhancing both shallow and deep magnetic source edges while equalizing anomaly amplitudes. Values near zero-mark contacts and shear zone boundaries (Salem *et al*., 2008). Positive values overlie magnetic sources; negative values occur off-source flanks. The map shows a highly textured pattern with dense, curvilinear zero contours trending predominantly NE-SW, reflecting intense structural deformation (Fairhead *et al*., 2004). Zero-crossing lineaments indicate prospective structural traps for magnetite-rich iron formations and pegmatite-related Ta-Nb-Li at intrusive contacts (Airo, 2015; Cooper & Cowan, 2006).

Analytical Signal (AS) Map

The analytic signal (AS) map (Figure 8) is characterized by values ranging from 0.01 to 0.23 nT/m. This filter calculates the total amplitude of the magnetic gradient, producing maxima directly over the edges and tops of magnetic source bodies regardless of magnetization direction, making it a robust tool for mapping geological contacts (Nabighian, 1972; Roest *et al*., 1992). Areas with high AS values, shown in pink and red colors, highlight high-amplitude geological features and are dominated in the eastern sectors, forming irregular, lobate clusters trending NE-SW. Low values prevail in the west. The sharp west-east transition in the AS amplitude marks a major tectonic contact or shear zone (Holden *et al*., 2008). These high-gradient regions show strong correlation with anomalies identified in the First Vertical Derivative (FVD) and Total Horizontal Derivative (THD) maps, confirming the location and structural significance of these prospective zones.

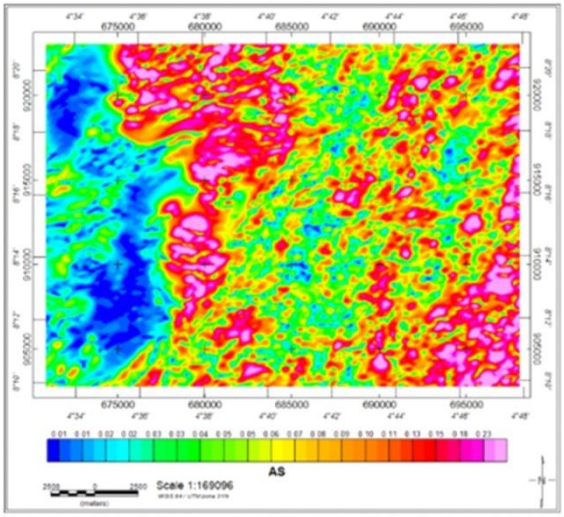

Figure 8: Analytical Signal (AS) map of the Study Area

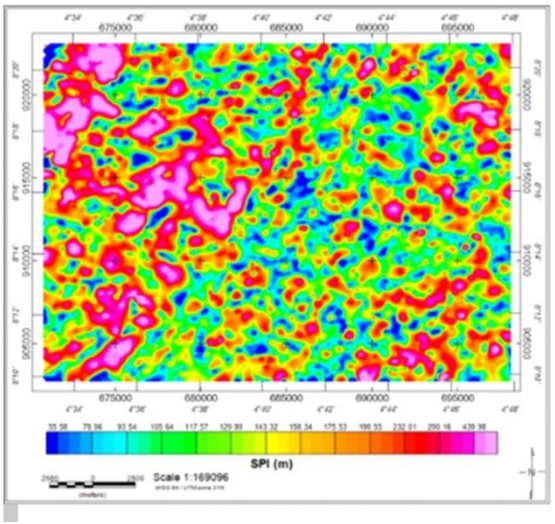

Figure 9: Source Parameter Imaging (SPI) map of the Study Area

Source Parameter Imaging (SPI)

The Source Parameter Imaging (SPI) map (Figure 9) with wavenumber derived from depth estimates ranging between 55.58 and 439.98 m. The SPI method estimates depths to the top of magnetic sources using local wavenumber analysis of the complex analytic signal, typically assuming simple geometrical models such as contacts or dikes (Thurston & Smith, 1997; Smith *et al*., 1998). High SPI values (>200 m) indicate deeper magnetic basement and are prevalent in the central-northern sectors, suggesting thicker overburden or a deeper weathering surface (Salem *et al*., 2005). In contrast, low SPI values (<150 m) mark shallow magnetic sources. These form irregular, lobate clusters trending NE-SW in the eastern and southern areas, suggesting that near-surface magnetized bodies—such as mafic intrusions, mineralized structures, or uplifted basement blocks—are a dominant feature in these zones (Airo, 2015; Hsu, 2002). The spatial correlation of these shallow-depth anomalies with high-amplitude analytic signal (AS) and high-gradient (THD/FVD) zones reinforces their interpretation as prospective targets for near-surface mineralization.

Euler Deconvolution

The Euler deconvolution map of the study area (Figure 10), derived from residual magnetic intensity data, estimates source depths using a structural index suitable for faults or dykes. The calculated depths range from about 60 m to over 338 m, with most solutions occurring between 100–250 m, indicating predominantly shallow magnetic sources (Mushayandebvu et al., 2001). The Euler solutions are widely distributed but show strong clustering in the southeastern (SE), central, northwestern (NW), and northeastern (NE) parts of the area, suggesting zones of shallow to intermediate-depth magnetic bodies. These clusters are interpreted as faults, fractures, and intrusive dykes, which may be associated with iron ore and other metallic mineralization. The solutions also display linear trends mainly oriented NE–SW, with secondary N–S, E–W, and NW–SE directions, consistent with the structural patterns observed in the FVD map and the Pan-African tectonic fabric of the Precambrian basement complex (Odeyemi et al., 1999). Overall, the distribution indicates a structurally complex basement terrain containing numerous shallow magnetic sources favorable for metallic mineral exploration (Reeves, 2005).

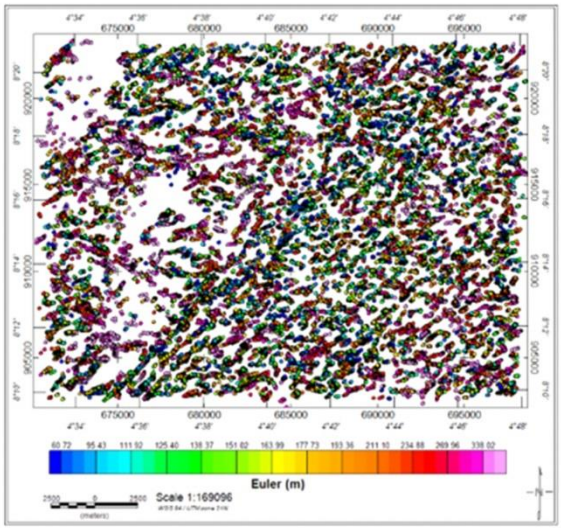

Figure 10: Euler Deconvolution map of the Study Area

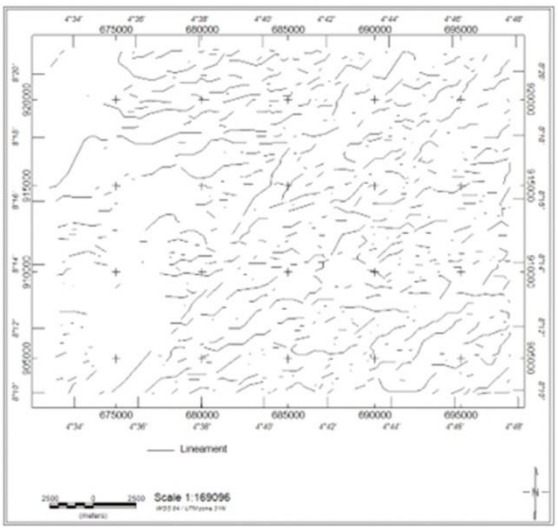

Figure 11: Lineament map of the Study Area

Lineament

The lineament map of the study area (Figure 11) delineates structural features such as faults, fractures, dykes, and lithological contacts extracted from magnetic and radiometric data, indicating a highly fractured Precambrian basement terrain. The dominant structural trend is NE–SW, consistent with the regional Pan-African tectonic fabric, while secondary trends include N–S, E–W, and NW–SE, forming a conjugate pattern typical of polyphase basement deformation (Kusky, 2004). Lineament density is highest in the northwest (NW), northeast (NE), and southeast (SE) parts of the study area, corresponding with zones of strong magnetic and radiometric anomalies. Prominent lineament intersections and clusters, particularly in the central and NW regions, indicate zones of intense deformation that enhance fluid migration pathways (Pérez-Peña et al., 2017). These structures act as conduits for hydrothermal fluids and sites of mineral deposition, explaining their association with iron ore and other metallic mineralization within fractures, faults, and dykes (Cox, 2005; Richards, 2003).

Structural Pattern

Geophysical structures were interpreted from the derivative and enhancement magnetic images. From the resulting rose diagram representing structural map, a significant number of lineaments (faults and fractures) with varying lengths were detected, indicating that the study area has been intensively fractured. These structures play a critical role in defining the tectonic architecture of the region. The orientation of these lineaments was statistically analyzed using a Rose Diagram (Figure 13). The diagram reveals a multi-modal structural distribution: Primary Trend: Linear structures of regional extent (> 5 km) mainly trend E-W (90°–270°) and NE-SW. The E-W trend is particularly dominant, showing the highest frequency of occurrences. Secondary Trends: In addition, short linear structures (< 1 km) displaying similar trends to the longer ones were also identified, alongside a minor NW-SE component. These orientations are consistent with the major tectonic events of the Nigerian Basement Complex, where the NE-SW and NNE-SSW trends represent the primary Pan-African grain, while the E-W features often represent later-stage brittle deformation and reactivation (Odeyemi, 1993; Anifowose, 2005).

Integration of Lineament and Euler Deconvolution

The integrated Euler Deconvolution and lineament analysis (Figure 12) of part of Ilorin Sheet 223 reveals a structurally complex terrain with significant mineralization potential. Shallow

Euler depth solutions (100–250m) cluster in the central (Alagbon) and southwestern (Aghogada) sectors, corroborating with major NE–SW and NW–SE lineaments. These intersection zones delineate high-strain corridors that focus hydrothermal fluids creating favorable conditions for polymetallic enrichment. The central corridor, with its dense fault intersections and shallow magnetic anomalies, could serve as potential mineralization of polymetallic mineral systems. The southwestern zone shows clustering of shallow solutions along NW–SE structures, suggesting iron oxide and sulfide concentrations linked to hydrothermal alteration. In contrast, the northeastern (Elesin funfun and Alayin) and southeastern (Erin Ile) domains exhibit deeper Euler solutions with structural intersections, reflecting magnetically uniform basement rocks and lower near-surface mineralization potential. Areas with moderate Euler depths that coincide with cross-cutting structures remain prospective for base metals (Pb–Zn–Cu) within secondary fractures and breccia zones. The spatial correlation between shallow Euler anomalies and structural intersections supports a model of structurally controlled polymetallic mineralization consistent with regional Pan-African tectonic overprinting and hydrothermal alteration.

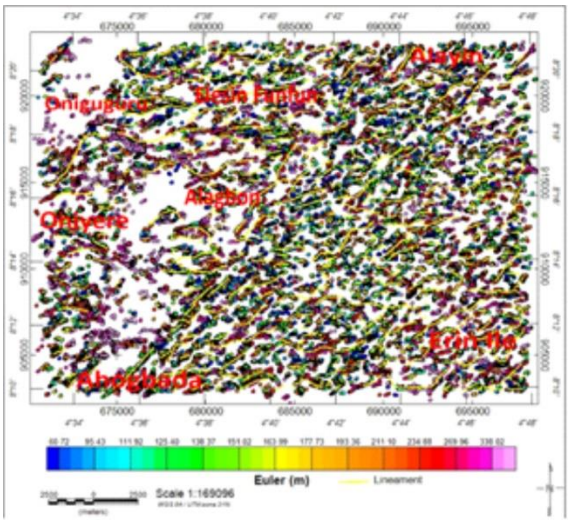

Figure 12: Integration of Euler and Lineament Map

Radiometric Result and Discussion

The radiometric method was employed to measure spatial variations in the mineral content of rocks within the study area. This aims to distinguish lithological units and identify zones of hydrothermal alteration. The technique is based on detecting gamma radiation emitted by naturally occurring radionuclides in rocks and soil. The principal radioactive elements measured are uranium (U), thorium (Th), and potassium (K), which occur as minor constituents in most rock-forming minerals and undergo natural radioactive decay, releasing gamma rays.

The potassium (K) distribution map of the study area (Figure 13) shows variable potassium concentrations that serve as indicators for distinguishing lithological units and alteration zones. Elevated potassium levels are often associated with rock alteration processes that can significantly increase K content (Wilford *et al*., 1997). The K-count map ranges from ~0.18 to 2.72 counts. Moderate to High K with pink/red colour is prominent in the northwest and central-west, often associated with K-feldspar-rich granites or potassic alteration. Low K with blue/cyan colour prevails in the east and southeast, suggesting mafic rocks, sediments, or depleted zones.

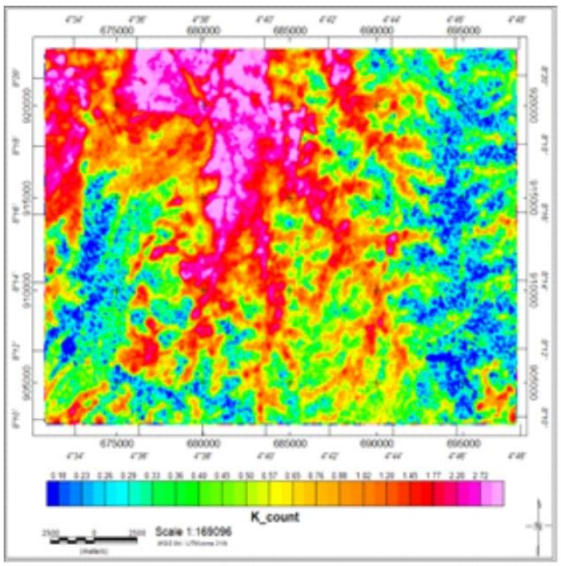

Figure 13: Potassium map of the Study Area

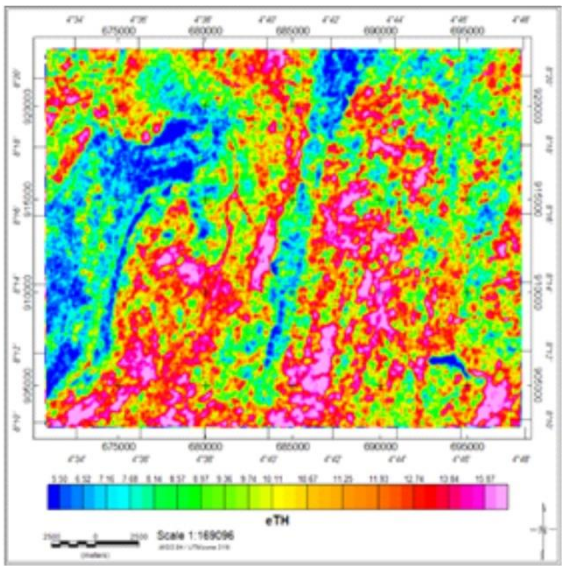

Figure 14: Thorium map of the Study Area

The Thorium (eTh) map (Figure 14) exhibits values ranging from 5.50 ppm (blue) to 15.87 ppm (pink/magenta), with most values between 8 and 14 ppm, consistent with statewide airborne surveys reporting Th from ~6.7 to >19 ppm in Kwara State (Adeyemo *et al*., 2025). The spatial distribution is markedly heterogeneous and patchy: High eTh anomalies (>12–15 ppm, red-pink) occur as Irregular, blob-like patches, dominant in the central and southern portions of the map. This corresponds to Th-enriched felsic intrusives. Low eTh zones (<8–10 ppm, blue-cyan) occupy the northwest and are expressed as prominent, narrow, linear to curvilinear features traversing the area. Thorium's low mobility in surficial environments means eTh primarily tracks primary lithological variations and accessory mineral content (e.g., monazite, allanite, thorite, zircon), IAEA 2003.

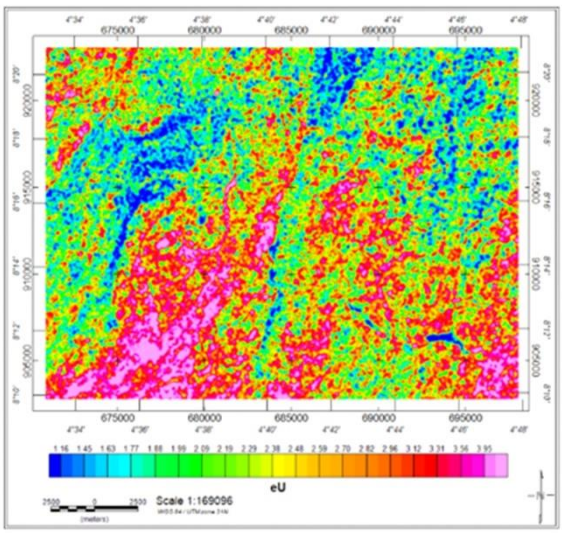

Figure 15: Uranium map of the Study Area

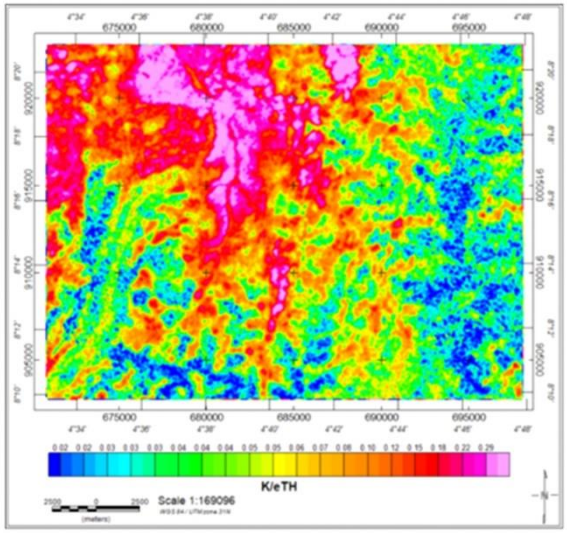

Figure 16: Potassium/Thorium ratio map of the Study Area

Figure 15 illustrates the Uranium map with values ranging between 1.16 ppm (blue) to 3.95 ppm (pink/magenta). The spatial distribution is highly heterogeneous and patchy, similar to the companion eTh map; High eU anomalies (>3–3.95 ppm, orange to pink): Irregular patches

scattered throughout the central and southern sectors which likely corresponds to U-enriched felsic granitoids or pegmatitic phases.
Low eU zones (<2 ppm, blue to cyan) prominent in northwestern areas and as narrow, curvilinear linear features across the map this indicate U-depleted lithologies (e.g., mafic rocks, quartzites, or schists).

K/eTh Ratio

The K/eTh ratio map (Fig. 16) shows values ranging from ~0.02 (blue) to 0.29 (pink/magenta), with high ratios (pink, red, magenta zones) widespread in the northwest, central-west, and parts of the southeast, indicating strong potassium enrichment relative to thorium. These anomalies typically signify potassic hydrothermal alteration, K-feldspar-rich granites, pegmatites, or related intrusions, often tied to fluid mobilization and mineralization pathways. Low ratios (blue/cyan zones) predominate in the east, northeast, and scattered southern areas, reflecting thorium-dominant signatures from resistant minerals in relatively unaltered felsic or mafic rocks. The elevated K/eTh zones align closely with structurally disrupted areas identified in magnetic, Euler, and lineament data, highlighting hydrothermal activity and structural control in migmatite-gneiss and granitic terrains—prospective settings for metallic mineralization such as iron ore, tantalite, or alteration-related deposits in fractured basement rocks. **The K/eU ratio map** (Fig. 17) displays values from ~0.06 (blue) to 1.35 (pink/magenta), with high ratios (pink, red, magenta) occurring extensively in the northwest, central-west, and scattered southeastern sectors, indicating pronounced potassium enrichment relative to uranium. These patterns are characteristic of potassic hydrothermal alteration, K-feldspar-rich granites/pegmatites, or zones where uranium has been leached and removed by mineralizing fluids. Low ratios (blue/cyan) dominate the eastern, northeastern, and some southern regions, indicating relative uranium enrichment (or reduced potassium mobility) in less-altered felsic rocks or areas that retain uranium-bearing accessory minerals. Both ratio maps reinforce structural and hydrothermal controls on radioelement distributions, enhancing prospects for targeted exploration in zones of alteration and faulting within the basement complex.

Ternary Map

The ternary radiometric map (Figure 18) is a composite RGB image showing the relative distribution of potassium (K – red), equivalent thorium (eTh – green), and equivalent uranium (eU – blue) in the study area (Minty, 2011). Magenta or purple zones, mainly in the east, southeast, and parts of the central area, indicate high K and eU relative to eTh and are typically associated with potassic, uranium-enriched felsic granites, pegmatites, or hydrothermal alteration zones (Wilford et al., 1997; Airo, 2015). Cyan to greenish zones, prominent in the northwest and central-west, reflect relatively higher eTh and K, suggesting the presence of thorium-bearing minerals, such as monazite, within granitic or gneissic rocks (Miles & Appleton, 2005). Red-dominated areas in the central and southern regions indicate strong potassium enrichment, commonly linked to K-feldspar-rich granites or potassic alteration. White or bright multicolored patches represent areas where all three radioelements are elevated, suggesting highly radiogenic felsic intrusions (Charbonneau & Smith, 1992). Overall, the pattern reflects lithological and structural controls, with high radioelement anomalies aligning with structurally complex zones identified from magnetic data, indicating exposed Precambrian basement rocks with possible hydrothermal alteration favorable for metallic mineralization (Anifowose, 2005).

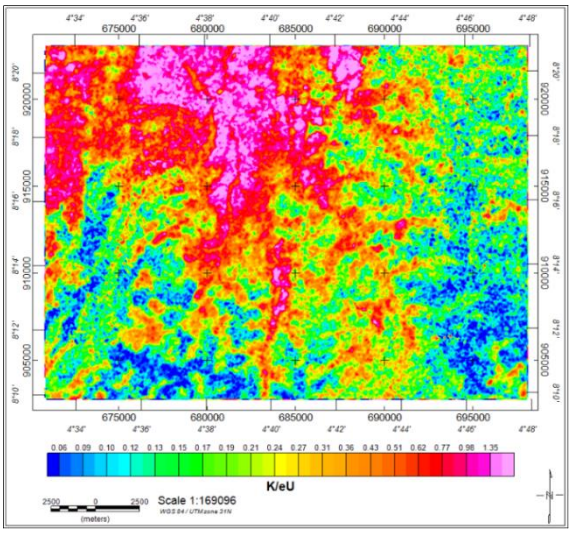

Figure 17: Potassium/Uranium ratio map of the Study Area

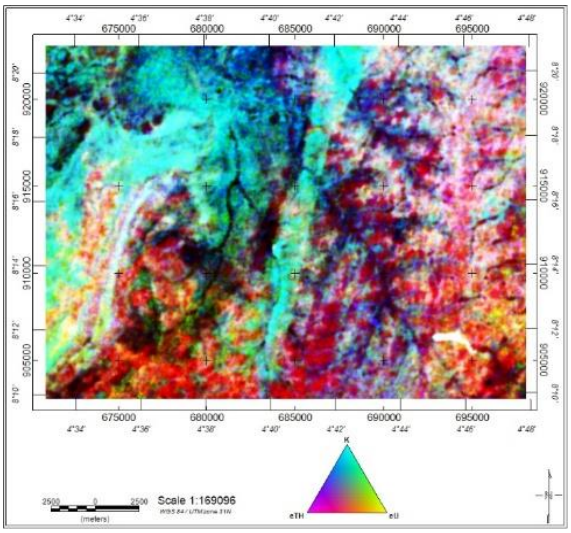

Figure 18: Ternary map of the Study Area

Data Analysis

Statistical tools play a crucial role in interpreting geochemical data by revealing patterns and anomalies more clearly. In this study, concentrations of 14 elements from 49 soil samples (appendix 1) were analyzed using both univariate and multivariate statistical methods, consistent with established approaches in the literature. Univariate analysis involved constructing histograms (using SPSS) for raw and log-transformed data to address the skewness typical of trace elements, from which descriptive statistics (mean, standard deviation) were calculated, and geochemical anomaly thresholds were set at mean + 2SD to identify potential anomalies. Multivariate techniques included Pearson correlation analysis (on both raw and log-transformed data) to assess inter-element relationships strong positive correlations indicating common sources, and negative ones suggesting antagonistic effects as well as R-mode factor analysis with varimax rotation and eigenvalue >1 criterion to reduce dimensionality, group elements into meaningful factors, and reveal underlying geochemical processes, sources, or associations relevant to mineral exploration and distinguishing geogenic from anthropogenic influences.

Results and Presentation

The findings from the statistical evaluation of data on the 13 trace elements determined in the soil samples in this study are presented and discussed below.

Table 1: Statistical summary of elements for the analysed soil geochemical data of the area.

Elements	Range of Metal Concentrations (ppm)	Arithmetic Mean (X)	Min	Max	Median	Standard Deviation (S)	Threshold (X+2S)	Coefficient of Variation
Li	2.42 - 16.32	7.51	2.42	16.32	6.93	3.57	14.65	0.48
Fe	1.01 - 17.92	6.63	1.01	17.92	5.54	4.85	16.33	0.73
Rb	4.10 - 40.70	22.15	4.1	40.7	23.4	9.33	40.8	0.42
Cs	0.32 - 4.38	1.53	0.32	4.38	1.14	0.93	3.39	0.61
Nb	3.30 - 41.80	20.87	3.3	41.8	19.6	10.5	41.87	0.5
Ta	0.45 - 16.31	3.32	0.45	16.31	2.65	2.91	9.15	0.88
Sn	0.50 - 3.30	1.77	0.5	3.3	1.7	0.7	3.18	0.4
Cu	3.30 - 85.90	24.07	3.3	85.9	19.2	18.39	60.85	0.76
U	0.80 - 5.50	2.15	0.8	5.5	1.9	0.98	4.11	0.45
Th	2.20 - 26.40	11.74	2.2	26.4	12.1	5.63	23.01	0.48
Pb	3.20 - 71.10	19.16	3.2	71.1	17.5	11.63	42.42	0.61
Zn	7.00 - 72.00	24.9	7	72	22	13.92	52.74	0.56
La	3.80 - 64.50	27.12	3.8	64.5	26.6	13.94	55	0.51

Table 2: Pearson correlation matrix of analyzed soil geochemical data of the study area

	Li	Fe	Rb	Cs	Nb	Ta	Sn	Cu	U	Th	Pb	Zn	La
Li	1												
Fe	0.08	1											
Rb	0.54	-0.18	1										
Cs	0.74	0.23	0.48	1									
Nb	0.61	0.03	0.65	0.59	1								
Ta	0.56	-0.04	0.4	0.57	0.66	1							
Sn	0.7	0.42	0.56	0.73	0.77	0.4	1						
Cu	0.26	0.84	0.06	0.4	0.23	-0.03	0.57	1					
U	0.31	0.79	0.12	0.37	0.28	0.19	0.64	0.61	1				
Th	0.15	0.5	0.37	0.31	0.41	0.14	0.54	0.46	0.57	1			
Pb	0.35	0.64	0.32	0.31	0.27	0.16	0.54	0.55	0.68	0.7	1		
Zn	0.23	0.61	0.06	0.43	0.19	-0.07	0.52	0.88	0.42	0.26	0.29	1	
La	0.19	0.41	0.43	0.39	0.52	0.11	0.63	0.57	0.41	0.85	0.5	0.5	1

Table 3: R-mode varimax rotated factor analysis

Element	Factor 1	Factor 2	Factor 3	Communality
Li	0.18	0.872	-0.0098	0.7928
Fe	0.8856	-0.0869	0.3067	0.8858
Rb	-0.2344	0.6697	0.4603	0.7154
Cs	0.3348	0.8232	0.0637	0.7937
Nb	-0.0182	0.8121	0.3707	0.7973
Ta	-0.1289	0.774	0.0388	0.6172
Sn	0.44	0.7183	0.4053	0.8737
Cu	0.9086	0.1378	0.2472	0.9056
U	0.6631	0.1998	0.4275	0.6624
Th	0.2546	0.1221	0.918	0.9225
Pb	0.4464	0.1725	0.6608	0.6656
Zn	0.8425	0.1844	0.0363	0.745
La	0.3136	0.2328	0.7851	0.769
Eigenvalue	3.5315	3.8604	2.7542	10.1461
Proportions of Total Variance (%)	27.17	29.70	21.19	78.05
Cumulative (%)	27.17	56.86	78.05	—

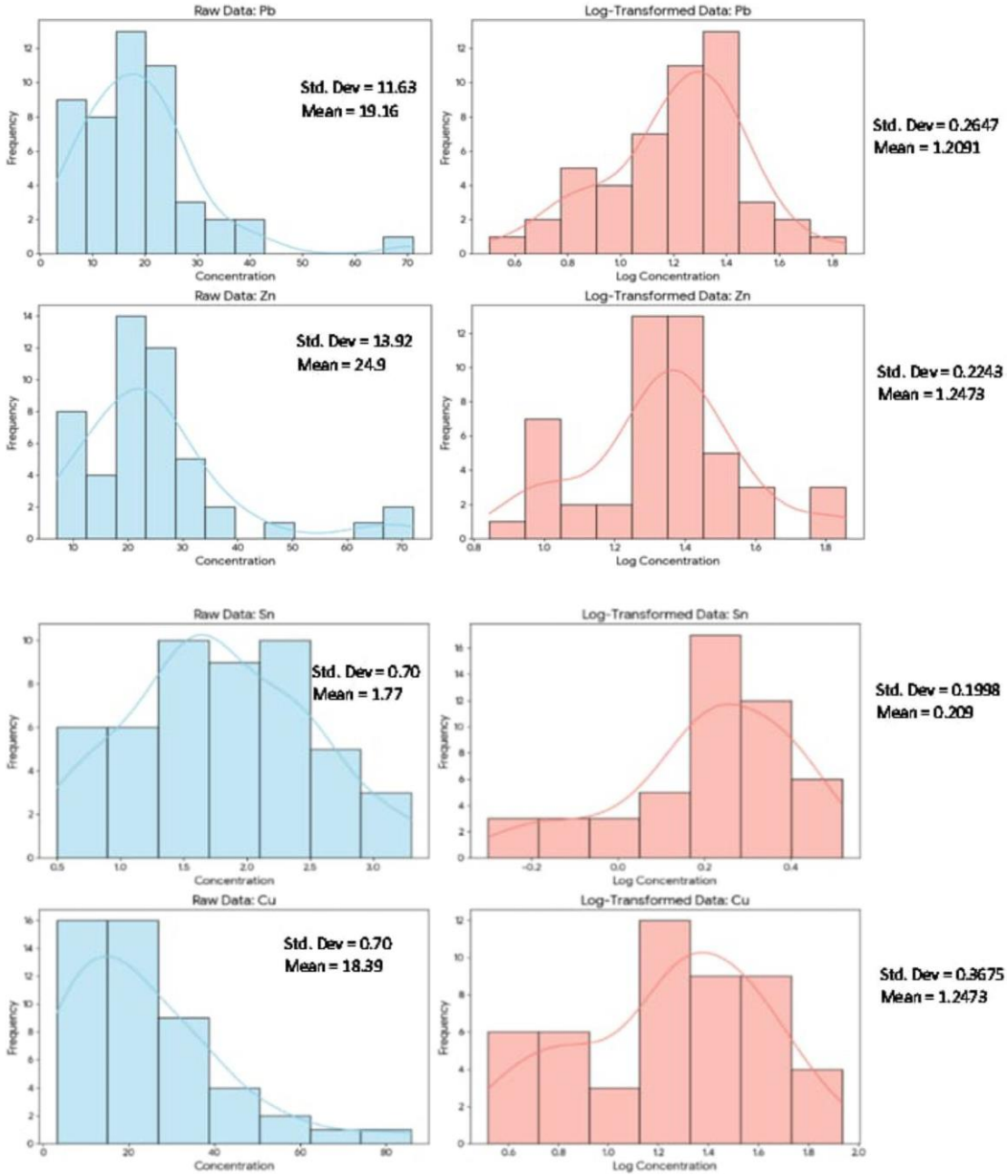

Figure 19: Representative frequency distribution diagrams of elements in the soils of the study area.

Frequency Distribution

Figure 19 shows the representative histograms of the frequency distributions. Table 1 presents the key summary statistics, including the element concentration range, mean, minimum, maximum, median, standard deviation, and threshold values. Visual examination of the histograms indicates that eleven of the thirteen elements—specifically Li, Rb, Cs, Nb, Ta, Cu, U, Th, Pb, Sn, and Zn are characterized by log-normal distributions. Among these, Cu, Pb, and Zn display pronounced positive skewness in their raw data histograms, whereas the remaining elements show mild skewness. The other two elements, Fe and La, assume a normal distribution. With the exception of tin (Sn), all histograms reveal discontinuities in their distributions, suggesting the presence of multiple overlapping populations.

The log-normal character of most elements is further confirmed by the near-symmetrical shapes observed in the log-transformed histograms, particularly for Pb, Zn, and Cu. These breaks in continuity, evident as bimodal or multimodal patterns in the raw data plots, likely reflect the superposition of background geochemical populations and localized anomalous enrichments. Identification of these multiple populations is critical for establishing reliable anomaly thresholds in geochemical exploration.

Pearson's 'r' Correlation

The correlation matrices were calculated for both raw and log-transformed datasets (Table 2), but the raw data were selected for final analysis and interpretation due to its near-identical patterns with the log-transformed results and its ability to produce sharper factor distinctions with fewer iterations in Varimax and Quartimax rotations (detailed comparisons appear in supplementary materials). Index 2 shows Pearson correlation coefficients ranging from -0.18 (Fe–Rb) to 0.88 (Cu–Zn), revealing diverse multi-element associations. Strong positive correlations ($r \geq 0.5$) occur within the lithophile rare-metal group (Li, Cs, Nb, Ta, Sn) and among Fe, Cu, Zn, U, Pb, Th, and La, likely reflecting primary magmatic mineralization and secondary adsorption processes. Moderate correlations ($0.3 \leq r < 0.5$) link Rb to several rare metals and connect certain base/transition metals with rare earth elements. A weak negative correlation between Fe and Rb ($r = -0.18$), together with other low values involving Ta, suggests opposing geochemical behaviors or distinct sources during late-stage magmatic evolution. Weak correlations ($r < 0.3$), including minor negative values, predominate between rare-metal lithophile elements (e.g., Li, Ta) and chalcophile/base-metal elements (e.g., Cu, Zn), indicating limited direct genetic linkage between these groups in parts of the study area. Overall, the correlation patterns point to multiple trace-element sources influencing the soil geochemistry.

Factor Analysis

The R-mode varimax rotated factor analysis (Table 3) of the geochemical dataset yielded a robust three-factor model that explains approximately 78.05% of the total variance and aligns well with the lithological and mineralization controls in the study area.

Factor 1 (27.17% variance) is dominated by strong positive loadings on Fe, Cu, Zn, and U, with moderate contributions from Pb and Sn. It represents a combined lithogenic and supergene enrichment process linked to mafic–intermediate basement rocks, hydrothermal activity, and lateritic weathering typical of tropical environments, in which Fe oxides/hydroxides act as scavengers for trace metals (Cu, Zn, Pb, U), and Sn indicates additional hydrothermal or altered-basement input. Factor 2 (29.7% variance), the strongest factor, groups Li, Cs, Nb, Ta, Sn, and Rb with high positive loadings, defining a classic lithophile rare-metal assemblage derived from primary magmatic fractionation in highly evolved granitic or pegmatitic melts. This reflects late-stage concentration of incompatible and large-ion lithophile elements, consistent with rare-metal pegmatites known in nearby regions. Factor 3 (21.19% variance) is characterized by high loadings on Th and La, together with significant Pb and U contributions. It represents a REE–radiogenic factor tied to accessory minerals (e.g., monazite, xenotime, allanite) in felsic rocks and their weathering products, capturing weathering-resistant residues enriched in thorium (immobile), uranium (moderately mobile), rare earth elements, and possibly radiogenic Pb from U–Th decay or minor sulfide mineralization.

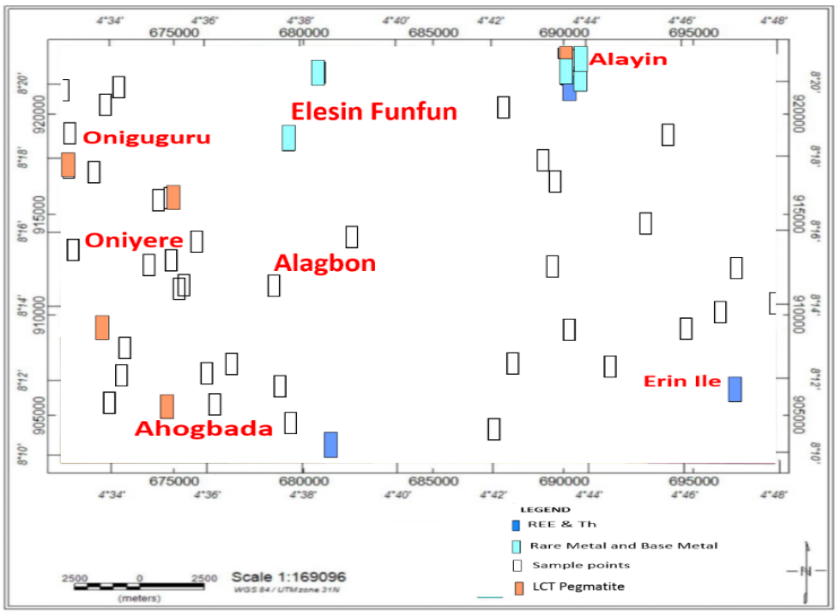

Figure 20: Potential mineralization map of the study area.

Figure 20 displays the visual potential mineralization map of the study area. Factor 1 (Fe-Cu-Zn-U) highlights a robust hydrothermal signature dominant around Elesin funfun and Alayin of the study area, in conjunction with a high-intensity cluster centered around Samples 38, 45, 46, 47 and 49. Factor 2 (Li-Cs-Nb-Ta-Sn-Rb) identifies a high-priority mineralisation zone characterised by a major linear structural control along the western margin consisting of Oniguguru, Oniyere, and Ahogbada in Samples 4, 17, 32, and 35, suggesting pegmatite emplacement. The highest prospectivity samples, 45 and 47, represent the most fractionated and enriched rare-metal signatures, marking them as primary targets for Lithium and Tantalum exploration.

Factor 3 (Th-La-Pb-U) reveals a distinct geochemical province in the Southeastern sector (Samples 1 and 7), trending from Erin Ile to Ahogbada, which hosts REE-bearing accessory minerals. The convergence of all three factors in the North-Eastern sector identifies it as the highest priority multi-commodity hotspot.

Discussion of Findings

The integration of geochemical, aeromagnetic, and aero-radiometric datasets provides a robust framework for assessing mineralization potential in part of Ilorin Sheet 223, Southwestern Nigeria, within the Nigerian Basement Complex. This approach reveals multifaceted controls on trace-element distributions, structural features, and alteration patterns, consistent with the polycyclic Pan-African orogeny, in which dominant NE–SW and NW–SE lineaments serve as conduits for fluid migration and mineral emplacement. Aeromagnetic enhancements (RTE, FVD, TDR, AS, SPI) delineate a structurally complex basement with heterogeneous TMI/RMI anomalies (−155 to +94 nT): high-amplitude positives in central-eastern sectors linked to mafic-ultramafic intrusions or magnetite-rich zones, and lows in western areas associated with felsic granites or demagnetized alteration. AS/THD edge detection and SPI shallow depths (11–142 m) in areas like Erin-Ile and Oniyere, combined with Euler deconvolution clustering shallow solutions (mostly 100–250 m) along lineaments, confirm structural controls on near-surface magnetic sources and mineralization potential, with lineament intersections acting as key fluid pathways. Aero-radiometric data complements this by mapping radioelement distributions: elevated K (up to 2.72 cps) and Th (up to 15.87 ppm) in central-southern areas indicate potassic alteration and Th-bearing accessories in pegmatites, while high K/Th and

K/U ratios highlight alteration zones. Ternary maps show magenta-purple signatures for K-U enriched granites/pegmatites and cyan-green for Th-dominant gneisses, correlating with magnetic lineaments and pointing to prospects for REE-LCT (lithium-cesium-tantalum) and uranium enrichment.

The integrated results support primary magmatic, supergene enrichment, and hydrothermal alteration processes aligned with regional metallogenic models, offering strong implications for targeted mineral exploration in structurally favorable zones of the Pan-African basement. The univariate analysis of 13 trace elements (Li, Fe, Rb, Cs, Nb, Ta, Sn, Cu, U, Th, Pb, Zn, La) in 49 soil samples demonstrates log-normal distributions for most elements, with pronounced positive skewness in Cu, Pb, and Zn, indicative of anomalous enrichments superimposed on background populations (Table 2). Frequency distribution histograms exhibit discontinuities or breaks, suggesting multiple overlapping populations from heterogeneous sources, including bedrock variations and secondary supergene processes in tropical weathering environments. The skewness normalizes upon log-transformation, supporting the presence of anomalous enrichments (Reimann *et al*., 2008).

Anomalies exceeding the threshold (mean + 2SD) are limited but significant, particularly for Ta (samples 22, 45), Sn (37, 47), Cu (38, 47), and Zn (37, 38, 47), suggesting subtle, dispersed enrichments. Elevated Ta (up to 16.31 ppm) and Nb (up to 41.8 ppm) in samples from Erin-Ile and Oniyere areas point to fractionated pegmatitic sources, consistent with LCT pegmatites in the Nigerian pegmatite belt (Černý & Ercit, 2005; Okunlola, 2005).

Pearson correlation matrices (Table 3) and correlation comparisons (Table 4) reveal strong positive associations ($r \geq 0.5$) among lithophile rare metals (Li-Cs r=0.74 raw, 0.83 log; Nb-Ta r=0.66 raw, 0.78 log) and chalcophile/base metals (e.g., Cu-Zn r=0.88 raw, 0.83 log; Fe-U r=0.79 raw, 0.83 log). These correlations strengthen upon log-transformation, underscoring the utility of normalization in mitigating skewness and enhancing linearity (Rollinson, 1993). The lithophile suite (Li, Cs, Nb, Ta, Sn, Rb) suggests primary magmatic fractionation from evolved granitic-pegmatitic melts, while the Fe-Cu-Zn-U-Pb-Th-La group implies secondary adsorption onto Fe-oxides during lateritic weathering (Rieuwerts, 2007; Hall & Silver, 2013). R-mode varimax factor analysis (Table 5) extracts three factors that account for 78.05% of the variance, with eigenvalues >1 (3.5315, 3.8604, 2.7542) and communalities generally >0.6 (e.g., 0.9225 for Th, 0.9056 for Cu), indicating a robust model with good variable representation. Factor 1 (27.17%; high loadings on Cu 0.9086, Fe 0.8856, Zn 0.8425, U 0.6631, with Pb 0.4464 and Sn 0.44) represents supergene enrichment in Fe-oxides/hydroxides, which scavenge trace metals under oxidizing tropical conditions (Emeh *et al*., 2019; Levinson, 1974). This aligns with hydrothermal Fe-mediated systems in basement terrains, where Cu-Zn anomalies indicate sulfide-bearing veins (Garba, 2003). Factor 2 (29.7%; Li 0.872, Cs 0.8232, Nb 0.8121, Ta 0.774, Sn 0.7183, Rb 0.6697) defines a classic rare-metal assemblage from LCT pegmatites, mirroring signatures in adjacent Kwara-Nasarawa fields (Ako, 1980; Akoh *et al*., 2015; Chukwu & Obiora, 2021). Factor 3 (21.19%; Th 0.918, La 0.7851, Pb 0.6608, U 0.4275) captures REE-radiogenic components from accessory minerals (e.g., monazite, xenotime) in felsic rocks, with Pb potentially from radiogenic decay or minor sulfides (Rose *et al*., 1979; Rollinson, 1993). The varimax rotation ensures orthogonal factors with clear geological interpretability, outperforming alternatives in distinguishing geogenic populations.

These geochemical patterns confirm polymetallic signatures, with LREE enrichment (∑REE up to 563 ppm; La up to 64.5 ppm) and Ta-Nb ratios supporting pegmatitic fractionation, while Cu-Zn-Fe anomalies (>60 ppm threshold for Cu) suggest base-metal sulfide systems. Integrating geochemistry with geophysics refines mineralization targeting. Factor 1

(hydrothermal signature) dominates around Elesin funfun/Alayin (samples 38, 45, 46, 47, 49), coinciding with shallow magnetic sources and high K/Th ratios, suggesting a core mineralizing system for base metals. Factor 2 (LCT assemblage) aligns with linear structures in Oniguguru/Oniyere/Ahogbada (samples 4, 17, 32, 35), indicating structurally controlled pegmatite emplacement for Li-Ta-Nb. Factor 3 (REE-Th) defines a southeastern province at Erin-Ile (samples 1, 7), overlapping with Th-U highs in ternary maps, pointing to localized REE enrichment in felsic intrusions. The convergence of factors in the north-eastern sector marks a multi-commodity hotspot. This multidisciplinary approach reduces false positives, as geophysical structures validate geochemical anomalies, and vice versa (El-Raouf *et al*., 2023; Xi *et al*., 2023). The outlined high-priority zones (Erin-Ile, Oniyere, Alayin) exhibit polymetallic potential within the SW-NE Nigerian rare-metal belt, with implications for lithium, Ta-Nb, and base metals amid global energy transitions (Upadhyay, 2025). This research aligns closely with recent explorations of pegmatites in Kwara State.

In summary, this study demonstrates that integrated geophysical and geochemical methods effectively delineate mineralisation potential in basement terranes, providing a scalable framework for sustainable exploration in Nigeria's mineral-rich belts. The identified zones warrant prioritized trenching and drilling to support economic development and resource security.

Conclusion

This integration of aeromagnetic, aeroradiometric, and soil geochemical data provides an effective approach for delineating mineralization potential in part of Ilorin Sheet 223, Southwestern Nigeria. The results reveal a structurally basement complex dominated by NE–SW and NW–SE lineaments with shallow magnetic sources (60–350 m), which act as conduits for mineralizing fluids. Radiometric analyses indicate zones of potassic enrichment and hydrothermal alteration associated with felsic and pegmatitic rocks, while geochemical data define three key mineralization signatures: LCT-type pegmatites (Li-Cs-Nb-Ta-Sn-Rb) and associated base-metal (Fe-Cu-Zn-U) and REE-Th-La-Pb enrichments. The integration of these datasets highlights high-priority polymetallic targets in the northeastern (Elesin-Funfun/Alayin), western (Oniguguru/Oniyere/ Ahogbada), and southeastern (Erin-Ile) sectors, controlled by structural intersections and alteration zones. This study provides a robust and reliable exploration framework that reduces target uncertainty and supports sustainable mineral resource development.

Reference

Abdelrady, A., El Kerni, K., Siddig, A., Abdellatif, M., & El Khadragy, A. (2023). Integrated geophysical methods for imaging saline karst aquifers: A case study of Stylos, Crete, Greece. Journal of Applied Geophysics, 208, 104877.

Adebayo, A.S., Ojo, A.O., & Kayode, J.S. (2023). Geophysical investigation of basement complex in southwest Nigeria. Journal of African Earth Sciences, 200, 104-110.

Adeyemo, I.A., Olatunji, A.S., & Fawale, O. (2025). Geospatial distributions of natural radioactivity in Kwara State, Nigeria using airborne gamma ray spectrometry data. Applied Water Science, 15, 1-15.

Airo, M.L. (2015). Aeromagnetic and aeroradiometric response to hydrothermal alteration. Surveys in Geophysics, 26, 273-299.

Ajakaiye, D.E., Hall, D.H., & Ashiekaa, J.A. (2019). Magnetic anomaly patterns over Nigeria and their geological significance. Tectonophysics, 760, 21-35.

Ajayi, T.R. (1981). Statistical analysis of stream sediment data from the Ife-Ilesa area, southwestern Nigeria. Journal of Geochemical Exploration, 15, 539-548.

Ako, B.D. (1980). A contribution to the geochemistry of the basement rocks of southwestern Nigeria. Nigerian Journal of Mining and Geology, 17, 129-138.

Ako, B.D., Onoduku, U.S., & Orazulike, D.M. (2015). Mineralization potentials of pegmatites in the Nasarawa area of central Nigeria. Earth Sciences Research Journal, 19, 101-111.

Anifowose, A.Y.B. (2005). Aeromagnetic mapping of basement structures and mineralization characterisation of Ilesa schist belt, southwestern Nigeria. Journal of Mining and Geology, 41, 143-149.

Ariyibi, E.A., Folami, S.L., Ako, B.D., Ajayi, T.R., & Omisore, B.O. (2010). Application of the principal component analysis on geochemical data: A case study in the basement complex of southern Ilesa area, Nigeria. Journal of Geophysics and Engineering, 8, 219-231.

Charbonneau, B.W., & Smith, J.R. (1992). Airborne radiometric surveys. In Exploration Geophysics (pp. 123-145). Kluwer Academic Publishers.

Chukwu, C.G. & Obiora, S.C. (2021). Petrogenesis and rare metal mineralization of the pegmatites in the Kwara-Nasarawa area, central Nigeria. Mineralogy and Petrology, 115, 141-159.

Cooper, G.R.J. & Cowan, D.R. (2006). Enhancing potential field data using filters based on the local phase. Computers & Geosciences, 32, 1585-1591.

Cox, S.F. (2005). Coupling between deformation, fluid pressures, and fluid flow in ore-producing hydrothermal systems at depth in the crust. Economic Geology, 100th Anniversary Volume, 39-75.

Černý, P. & Ercit, T.S. (2005). The classification of granitic pegmatites revisited. Canadian Mineralogist, 43, 2005-2026.

Dada, S.S. (1998). Crust-forming ages and Proterozoic crustal evolution in Nigeria: A reappraisal of current interpretations. Precambrian Research, 87, 65-83.

Ebele, C.P., Ogunyele, A.C., & Mallam, A. (2025). Aeroradiometric data for lithological mapping and alteration zones in basement terrains. Journal of African Earth Sciences, 211, 105-115.

Ekwume, B.N., Ntekim, E.E., & Emeh, J.U. (1995). The geochemistry of ultramafic rocks of the Obudu Plateau, southeastern Nigeria. Journal of Mining and Geology, 31, 25-33.

El-Omairi, M.A., Eldosouky, A.M., & Abdelrahman, K. (2025). Role of mineral resources in energy transition and industrial development. Renewable and Sustainable Energy Reviews, 189, 113-125.

El-Raouf, A.A., El-Wardany, R.M., Abdelrahman, K., & Shebl, A. (2023). Integration of geochemical and geophysical data for mineral exploration in basement terrains. Minerals, 13, 600.

Emeh, C., Onuba, L., & Orazulike, D.M. (2019). Geochemical signatures of supergene enrichment in basement-derived materials. Journal of Geochemical Exploration, 201, 105-115.

Fairhead, J.D., Salem, A., & Williams, C. (2004). Structural mapping using aeromagnetic data in low latitudes. SEG Technical Program Expanded Abstracts, 23, 605-608.

Fairhead, J.D., Salem, A., Cascone, L., Hammill, M., Masterton, S., & Sampson, E. (2017). New developments of the magnetic tilt-depth method to improve structural mapping of sedimentary basins. Geophysical Prospecting, 59, 1072-1086.

Garba, I. (2003). Geochemical discrimination of gold mineralization in Nigeria. Journal of Mining and Geology, 39, 91-102.

Gloss, D.L., Cochran, J.R., & Bowin, C. (1975). The use of factor analysis in geophysical data interpretation. Geophysics, 40, 105-115.

Grant, F.S. (1985). Aeromagnetics, geology and ore environments, I. Magnetite in igneous, sedimentary and metamorphic rocks: An overview. Geoexploration, 23, 303-333.

Gunn, P.J., Fitzgerald, D., Yassi, N., & Dart, P. (2022). New developments in the analytic signal technique for interpretation of aeromagnetic data. Exploration Geophysics, 53, 245-255.

Hall, G.E.M. & Silver, M. (2013). Trace element adsorption on iron oxides in soils. Applied Geochemistry, 33, 80-90.

Holden, E.J., Dentith, M., & Kovesi, P. (2008). Towards the automated analysis of regional aeromagnetic data to identify regions prospective for gold deposits. Computers & Geosciences, 34, 1505-1522.

Hsu, S.K. (2002). Imaging magnetic sources using Euler's equation. Geophysical Prospecting, 50, 15-25.

IAEA. (2003). Guidelines for radioelement mapping using gamma ray spectrometry data. IAEA-TECDOC-1363, International Atomic Energy Agency.

Jahantigh, H., Eldosouky, A.M., & Pour, A.B. (2025). Aeroradiometric data for hydrothermal alteration mapping. Ore Geology Reviews, 160, 105-115.

Kanmi, A.A., Olatunji, A.S., & Adeoti, L. (2024). Structural controls on groundwater flow in basement terrains. Hydrogeology Journal, 32, 1001-1015.

Kusky, T. (2004). Precambrian ophiolites and related rocks. Developments in Precambrian Geology, 13, 1–35.

Levinson, A.A. (1974). Introduction to exploration geochemistry. Applied Publishing Ltd.

Miles, J.C.H. & Appleton, J.D. (2005). Mapping variation in radon potential both between and within geological units. Journal of Radiological Protection, 25, 257–276.

Minty, B. (2011). Airborne radiometric mapping. In Airborne Geophysics (pp. 201–215). Springer.

Mushayandebvu, M.F., van Driel, P., Reid, A.B., & Fairhead, J.D. (2001). Magnetic source parameters of two-dimensional structures using extended Euler deconvolution. Geophysics, 66, 814-823.

Nabighian, M.N. (1972). The analytic signal of two-dimensional magnetic bodies with polygonal cross-section: Its properties and applications to automated anomaly interpretation. Geophysics, 37, 507-517.

Nabighian, M.N. (1984). Toward a three-dimensional automatic interpretation of potential field data via generalized Hilbert transforms: Fundamental relations. Geophysics, 49, 780-786.

NGSA. (2010). Airborne geophysical surveys in Nigeria. Nigerian Geological Survey Agency Report.

Odeyemi, I.B. (1993). A comparative study of remote sensing images of the structure of Okemesi fold belt, Nigeria. International Journal of Remote Sensing, 14, 2503-2515.

Odeyemi, I.B., Anifowose, A.Y.B., & Asubiojo, O.I. (1999). Multi-technique structural analysis of the western part of the Ilesa schist belt, southwestern Nigeria. Journal of Mining and Geology, 35, 101-110.

Okunlola, O.A. (2005). Metallogeny of tantalum-niobium mineralization of Precambrian pegmatites of Nigeria. Mineral Wealth, 137, 38-50.

Okunlola, O.A. (2008). Compositional characteristics of rare-metal pegmatites in southwestern Nigeria. Journal of Mining and Geology, 44, 123-136.

Okunlola, O.A., Oyedokun, M.O., & Olaitan, O.M. (2022). The Nigerian basement complex: A review. Earth Science Research Journal, 26, 1–15.

Okunlola, O.A. & Somorin, E.B. (2006). Compositional features of Precambrian pegmatites of Ago-Iwoye area, southwestern Nigeria. Journal of Mining and Geology, 42, 71-77.

Oyeniyi, A.P., Adegoke, O.S., & Layade, G.O. (2016). Aeromagnetic study of basement structures in central Nigeria. Journal of Applied Geophysics, 135, 357-364.

Partington, G.A. & Williams, P.J. (2000). Proterozoic lode gold and (iron) copper-gold mineralization: A comparison of two contrasting provinces. Economic Geology, 95, 691-713.

Pérez-Peña, J.V., Azañón, J.M., Azor, A., Delgado, J., González-Lodeiro, F., & Booth-Rea, G. (2017). Quaternary strike-slip dextral faulting as the cause of the Central Betics fold pattern: Insights from deformation experiments and geomorphic data. Tectonophysics, 707, 81-94.

Phillips, J.D. (2002). Processing and interpretation of aeromagnetic data for the Santa Cruz Basin - Patagonia Mountains area, south-central Arizona. U.S. Geological Survey Open-File Report 02-98.

Rahaman, M.A. (1988). Recent advances in the study of the basement complex of Nigeria. In Precambrian Geology of Nigeria (pp. 11-43). Geological Survey of Nigeria.

Reid, A., Ebbing, J., & Webb, S. (2021). Avoidable Euler errors – the use and abuse of Euler deconvolution applied to potential fields. Geophysical Prospecting, 69, 1756-1778.

Reimann, C., Filzmoser, P., Garrett, R.G., & Dutter, R. (2008). Statistical data analysis explained: Applied environmental statistics with R. John Wiley & Sons.

Reeves, C. (2005). Aeromagnetic surveys: Principles, practice & interpretation. Geosoft Inc.

Richards, J.P. (2003). Tectono-magmatic precursors for porphyry Cu-(Mo-Au) deposit formation. Economic Geology, 98, 1515-1533.

Rieuwerts, J. (2007). The elements of environmental pollution. Routledge.

Roest, W.R., Verhoef, J., & Pilkington, M. (1992). Magnetic interpretation using the 3-D analytic signal. Geophysics, 57, 116-125.

Rollinson, H. (1993). Using geochemical data: Evaluation, presentation, interpretation. Longman Scientific & Technical.

Rose, A.W., Hawkes, H.E., & Webb, J.S. (1979). Geochemistry in mineral exploration. Academic Press.

Salem, A., Ravat, D., Mushayandebvu, M.F., & Ushijima, K. (2005). Linearized least-squares method for interpretation of potential-field data from sources of simple geometry. Geophysics, 70, L1-L5.

Salem, A., Ravat, D., Smith, R., & Ushijima, K. (2007). Fourier-domain magnetic source parameters estimation using least-squares inversion. Geophysical Prospecting, 55, 685-697.

Salem, A., Ravat, D., Gamey, T.J., & Ushijima, K. (2008). Analytic signal approach and its applicability in environmental magnetic investigations. Journal of Applied Geophysics, 61, 292-300.

Shereif, H.M., Eldosouky, A.M., & Abdelrahman, K. (2025). Aeromagnetic data for structural mapping and mineralization. Ore Geology Reviews, 160, 105-115.

Smith, R.S., Thurston, J.B., Salem, A., & Reid, A.B. (1998). A comparison of airborne EM inversion methods for the recovery of conductivity and susceptibility. SEG Technical Program Expanded Abstracts, 17, 1476-1479.

Tanko, I.Y., Adamu, C.I., & Umaru, B. (2024). Mineral occurrences in the Nigerian basement complex. Journal of Mining and Geology, 60, 45-58.

Thurston, J.B. & Smith, R.S. (1997). Automatic conversion of magnetic data to depth, dip, and susceptibility contrast using the SPI(TM) method. Geophysics, 62, 807–813.

Upadhyay, R. (2025). Limitations of conventional exploration in complex terrains. Mineralium Deposita, 60, 1-15.

Wilford, J.R., Bierwirth, P.N., & Craig, M.A. (1997). Application of airborne gamma-ray spectrometry in soil/regolith mapping and applied geomorphology. AGSO Journal of Australian Geology and Geophysics, 17, 201-216.

Xie, Y., Hou, Z., Goldfarb, R.J., Guo, X., & Wang, L. (2023). Geochemical methods for mineral exploration. Economic Geology, 118, 1-25.